Wave and Turbulence Structure in a Shallow Baroclinic Convective Boundary Layer and Overlying Inversion

MING YU ZHOU,[1] D. H. LENSCHOW AND B. B. STANKOV

National Center for Atmospheric Research,[2] Boulder, CO 80307

J. C. KAIMAL AND J. E. GAYNOR

NOAA/ERL/Wave Propagation Laboratory, Boulder, CO 80303

(Manuscript received 25 June 1984, in final form 28 September 1984)

ABSTRACT

Data from the Boulder Atmospheric Observatory (BAO) are used to investigate the wave and turbulence structure of the convective atmospheric mixed layer and the overlying inversion. Three cases are discussed, one in considerable detail, in which the depth of the mixed layer is below the top of the 300 m tower at the BAO and is nearly steady state for several hours. Velocity and temperature variances and spectra, coherences between vertical velocity and temperature, and vertical velocities at different levels on the tower are used to show that although the mixed-layer behavior is for the most part similar to that found in previous studies, there are some significant differences due mainly to the relatively large shear term in the turbulence energy equation compared with buoyancy, both within the mixed layer and in the capping inversion. For example, the wavelength of the spectral maximum for vertical velocity in the upper half of the mixed layer is about three times the boundary-layer height, which is about twice that estimated in a previous experiment. The wavelength is up to 5.5 times the mixed-layer height above the top of the mixed layer. Within the mixed layer, terms in the turbulence kinetic energy equation are similar to previous studies. Above the mixed layer, shear production becomes large, and is approximately balanced by the sum of the buoyancy, dissipation and transport terms. The temperature variance and flux budgets also have large terms and significant residuals in the overlying inversion.

1. Introduction

Recent studies of the atmospheric convective boundary layer have provided much useful information on the structure of the surface layer and the mixed layer, but less information on the structure near the top of the mixed layer. Kaimal *et al.* (1976), for example, reported in considerable detail the behavior of turbulence statistics from the surface layer to well into the overlying mixed layer. Lenschow (1974) and Caughey and Wyngaard (1979) reported measurements of the turbulence kinetic energy budget throughout the mixed layer. Lenschow *et al.* (1980) analyzed the budgets of turbulence kinetic energy, temperature, and humidity variance and fluxes of temperature and humidity throughout a baroclinic mixed layer, but with little detail in the vicinity of the capping inversion. One of the few observational studies of turbulence structure near the top of the mixed layer was carried out by Caughey and Palmer (1979). Wyngaard and LeMone (1980) have investigated the effects of entrainment on the variance of scalars in the upper part of the mixed layer.

In this paper we analyze the structure of turbulence throughout the convective boundary layer, including the capping inversion and the layer just above it. The major focus of the study is the region near the top of the mixed layer and its relation to the underlying predominantly buoyancy-driven turbulent layer. The boundary layer considered here is not a typical convective boundary layer—it is shallower and more baroclinic than most. As a result, vertical wind shear and the effects of the overlying inversion play a relatively more important role. It is likely, however, that the basic mechanisms are similar to those in other boundary layers, so that the results obtained here apply also to more typical convective boundary layers.

We use data from the Boulder Atmospheric Observatory (BAO), which is located about 25 km east of the foothills of the Rocky Mountains in Colorado. The tower instrumentation is described by Kaimal and Gaynor (1983). Briefly, a three-axis sonic anemometer, a propeller-vane anemometer, a quartz thermometer, and a cooled-mirror dewpoint hygrom-

[1] Present affiliation: Institute of Atmospheric Physics, Academia Sinica, Beijing, China.

[2] The National Center for Atmospheric Research is sponsored by the National Science Foundation.

eter are mounted at each of eight levels (10, 22, 50, 100, 150, 200, 250 and 300 m above the ground). In addition, a movable carriage containing the same array of instruments, except for a Lyman-alpha hygrometer in place of the dewpoint hygrometer, is available on the tower for obtaining continuous vertical soundings. Two acoustic sounders and a network of five sensitive microbarographs that can be used to detect the phase speed and direction of propagating internal waves are arrayed near the tower.

After sunrise the convective boundary layer typically develops quickly to a depth beyond the top of the tower. Occasionally, however, when the capping inversion is strong and subsidence is large, the convective boundary layer grows so slowly that the capping inversion remains below the top of the tower. We have selected three cases for which this is true and for which no significant changes in the weather occurred at the site: 27 March 1981, 27 March 1982 and 25 February 1983. We then investigate in detail the first of these cases since the most data are available for that day. On all of these days, relatively cool air was advected into the area from the northeast, moving upslope. An occasional layer of thin stratus clouds drifted past the tower at the top of the mixed layer. The clouds were never thick enough to completely obscure the sun, although incoming radiation was reduced at the surface. There is no indication that the presence of these clouds affected the structure of the temperature field. This situation occurs with a low-pressure area to the south and a cold air mass pushing into the midwest from the north. The result is a very shallow baroclinic boundary layer at the BAO. Nieuwstadt (1983) discusses the role of boundary-layer depth and baroclinity on the wind and stress profiles and shows that shallower boundary layers should be expected to have a larger velocity jump across the top than do deeper boundary layers. Therefore, these are cases in which wind shear is a more important consideration in the turbulence kinetic energy budget than it is in typical convective boundary layers—particularly near the top of the mixed layer.

The cases studied here bear some similarity to the situation occurring over the East China Sea during wintertime cold air outbreaks, as studied during the Air Mass Transformation Experiment (AMTEX), except that baroclinic effects are even more significant and the boundary layer is shallower for the cases considered here. Mahrt (1981) and Jensen and Lenschow (1978) examined the entrainment process and the scale of the turbulence near the overlying inversion using aircraft observation from AMTEX. Although shear is important at the top of the AMTEX boundary layer, it is not as dominant as it is here.

2. Discussion of cases

Figure 1 shows the temperature and wind velocity profiles from the fixed levels and the temperature profile from the movable carriage for the 27 March 1981 case. The movable carriage results, which are obtained from an average of four soundings over an hour, show that the capping inversion is between 175 and 250 m, and its strength is about 6°C/100 m. Above 250 m the inversion weakens to about 1°C/100 m. Between 100 m and the inversion base, the boundary-layer lapse rate is slightly stable; below this, it is nearly neutral to slightly unstable. This structure is characteristic of convective boundary layers. A minimum in wind speed and a maximum in wind shear occur at 250 m; above this the wind direction rotates from north to southwest.

Profiles of temperature and wind velocity for the other two cases are similar to these and are not shown.

3. Variances

Variances of the velocity components and temperature, and Richardson number for all three cases are

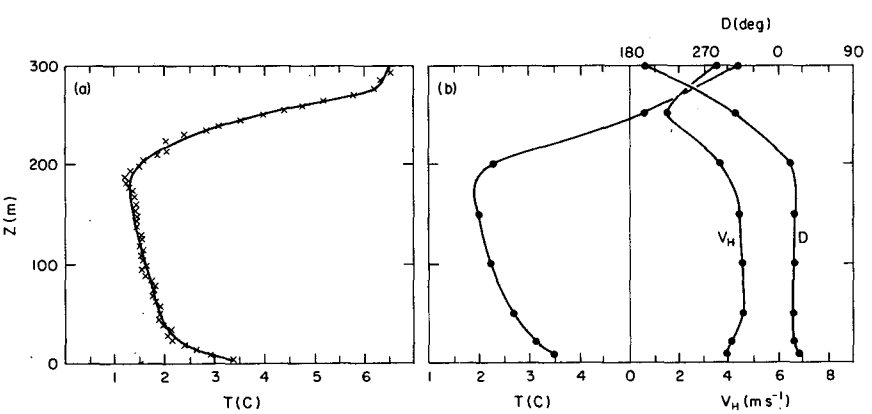

FIG. 1. Profiles of temperature and horizontal wind velocity from 0840 to 0940 MST (Mountain Standard Time) for 27 March 1981, (a) observed by movable carriage and (b) observed from fixed levels on the tower.

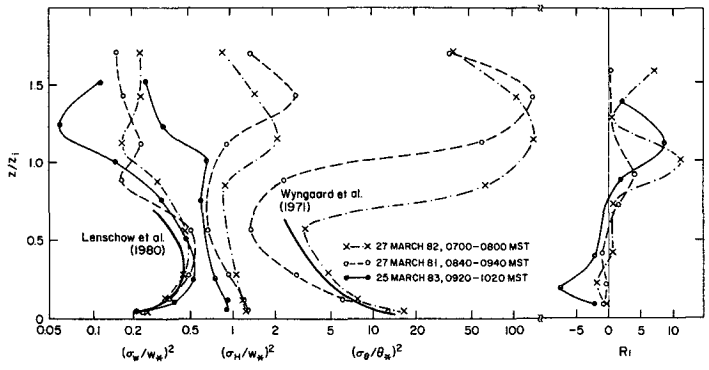

FIG. 2. Vertical distribution of normalized variances of velocities and temperature, and Richardson number.

shown in Fig. 2. The variances are calculated from averages of three 20 min periods, with a sampling rate of 10 s^{-1}, and then normalized by the mixed-layer velocity and temperature scales,

$$w_*^3 = \frac{g}{T} z_i (\overline{w\theta})_s, \tag{1}$$

$$\theta_* = \frac{(\overline{w\theta})_s}{w_*}, \tag{2}$$

where g/T is the buoyancy parameter, $(\overline{w\theta})_s$ is the surface temperature flux obtained from extrapolation of the tower-measured flux profile to the surface, and z_i is the mixed-layer depth. Several definitions of z_i have appeared in the literature. Caughey and Palmer (1979) and Kaimal *et al.* (1976) define z_i as the height of the inversion base capping the mixed layer, while others (e.g., Wyngaard and LeMone, 1980) define it as the minimum of the virtual temperature flux. We use the first of these definitions.

In most cases, the two definitions of z_i yield comparable values. This boundary layer is not typical; the second definition leads to an inversion height that is about 30% greater. Our time traces of temperature, humidity, and wind components show distinctly different flow regimes above and below the inversion base: undulating motions above and turbulent fluctuations characteristic of a convective boundary layer below. No discernible transition occurs at the level where the virtual temperature flux reaches its minimum value.

The boundary-layer scaling parameters for all three cases are shown in Table 1. In the lower and middle part of the mixed layer, the normalized vertical velocity variance σ_w^2/w_*^2, shown in Fig. 2, increases with height as expected (Caughey and Wyngaard, 1979; Lenschow *et al.*, 1980), even though the mixed layer is relatively shallow. Below 0.7 z_i the variance agrees with the curve suggested by Lenschow *et al.* (1980):

$$\frac{\sigma_w^2}{w_*^2} = 1.8\left(\frac{z}{z_i}\right)^{2/3}(1 - 0.8z/z_i)^2. \tag{3}$$

Near the top of the mixed layer, the structure is more complicated in that a minimum occurs near z_i.

The Richardson number is defined by

$$\mathrm{Ri} = \frac{g}{T}\frac{\Delta\Theta_v/\Delta z}{(\Delta U/\Delta z)^2 + (\Delta V/\Delta z)^2}, \tag{4}$$

where U and V are the mean horizontal wind components along the x (east) and y (north) axes, respectively, Θ_v is the virtual potential temperature, and Δ denotes a difference over a finite height increment Δz. The fluctuating components u and v are also defined along the x and y axes, respectively. It is seen in Fig. 2 that the maximum value of Ri occurs near the base of the capping inversion. Thus, the vertical variance is inhibited by the very stable stratification near z_i, but above z_i, variance due to both waves and turbulence may be generated by the wind shear.

TABLE 1. Boundary-layer parameters. For the 25 February 1983 case, u and v data are missing at z = 10 m.

Date	Time (MST)	u_* (m s^{-1})	$-L$ (m)	z_i (m)	w_* (m s^{-1})	θ_* (°C)	$(\overline{w\theta})_s$ (m s^{-1} °C)
27 March 1981	0840–0940	0.29	16.2	175	0.93	0.147	0.136
27 March 1982	0700–0800	0.12	10.7	175	0.41	0.028	0.012
25 February 1983	0920–1020	—	—	200	0.84	0.108	0.094

The horizontal velocity variance

$$\frac{\sigma_H^2}{w_*^2} = \frac{1}{2}\left(\frac{\sigma_u^2 + \sigma_v^2}{w_*^2}\right) \tag{5}$$

is also shown in Fig. 2. The mixed-layer values are consistent with, although somewhat larger than, the results of Lenschow *et al.* (1980) and Caughey and Wyngaard (1979). A significant maximum occurs near or above z_i, which is also clearly shown in Moeng (1984) numerical results. We find that in the middle of the mixed layer the horizontal and vertical variances are similar in magnitude. Above z_i the horizontal variance is considerably greater than the vertical variance.

Figure 2 shows that for two of the cases the normalized temperature variance $\sigma_\theta^2/\theta_*^2$ decreases with height up to the middle of the mixed layer, then increases with height to a maximum value above z_i. The third case, 25 February 1983, is not included because some data are missing. Near the surface, the variance is fairly well represented by the free-convection prediction of Wyngaard *et al.* (1971),

$$\frac{\sigma_\theta^2}{\theta_*^2} = 1.8\left(\frac{z}{z_i}\right)^{-1/3}. \tag{6}$$

Above z_i the temperature variance maximum is larger than that observed in the Ashchurch experiment (Caughey and Wyngaard, 1979). Moeng and Wyngaard (1984) obtained numerical results that show that near the top of the mixed layer temperature variance increases with increasing magnitude of the ratio of entrainment flux to surface flux. In our cases, however, the maximum seems to be the result mainly of the internal waves and turbulence, which produce vertical displacements of the strong inversion layer.

From the above observations, we can conclude that the turbulent structure of these shallow mixed layers is likely to be similar to that reported in other studies of mixed-layer structure (Kaimal *et al.*, 1976). This leads us to believe that the turbulence structure in the overlying stratified layer may also be of general significance.

4. Wave motion and spectra

The acoustic sounder record for 0600–1030 MST on 27 March 1981 is shown in Fig. 3. After 0700 MST, the echo indicates increasing convective activity near the surface, while z_i, on the average, remains almost stationary. Throughout the period shown in Fig. 3 we see oscillations in echo heights of several tens of meters amplitude with periods of several minutes within the mixed layer and several tens of minutes at the capping inversion. Figure 4 shows all four profiles obtained from the movable carriage between 0840 and 0940 MST on 27 March 1981, relative to the mid-mixed-layer temperature at 100 m. We see that the temperature variation in the mixed layer is somewhat less than 1°C, and that the height of the capping inversion varies by about 50 m during this time. The inversion height variations typically result from a combination of thermal penetrations and wave activity. Mahrt (1979) reviewed much of the previous work on penetrative convection at the top of a convective boundary layer, and tried to estimate the penetration depth of convective elements at the top of the mixed layer. Using his formulations for penetration depth of convective elements we estimate a value of only a few meters. Therefore, wave activity seems to be the dominant source of the observed inversion height variations.

We used the BAO "beamsteering" program (Young and Hoyle, 1975), which requires a minimum of an

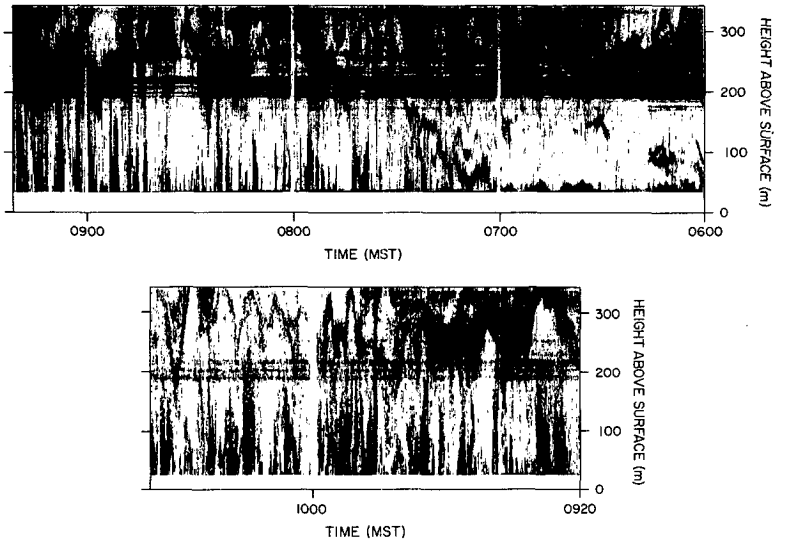

FIG. 3. Acoustic sounder record on 27 March 1981.

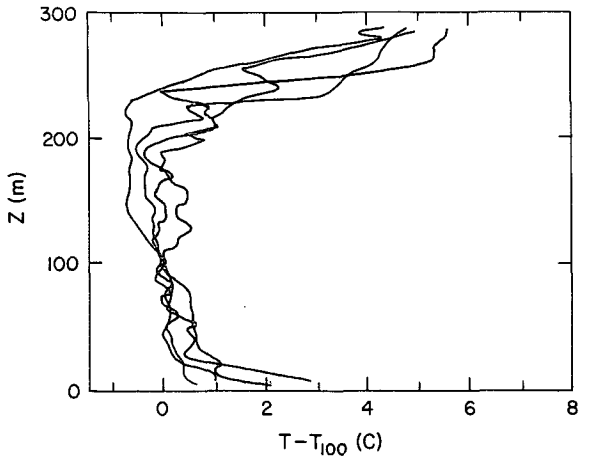

FIG. 4. The temperature profiles observed by the movable carriage for 0840–0940 MST 27 March 1981.

80 min time series from the microbarograph array, to calculate the phase speed and direction of the waves. The results are shown in Fig. 5; the points are plotted at the middle of the time period and are obtained by incrementing the starting time by 20 min. Prior to 0740 MST the first component f_1 dominates for each 80 min calculation. This appears as a peak at $\sim 4 \times 10^{-4}$ Hz in the spectral density plot shown in Fig. 6a for 0720 MST on 27 March

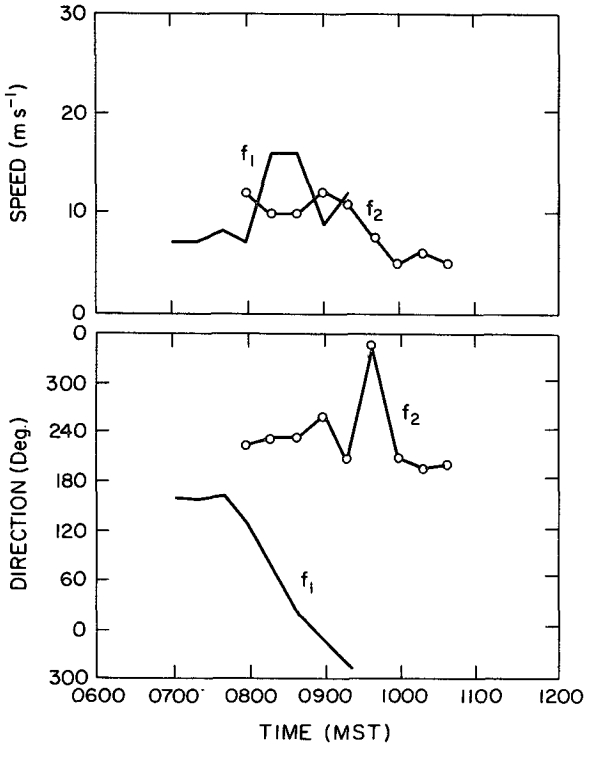

FIG. 5. Wave phase speed and direction calculated at 20 min intervals from 0700 to 1040 MST 27 March 1981.

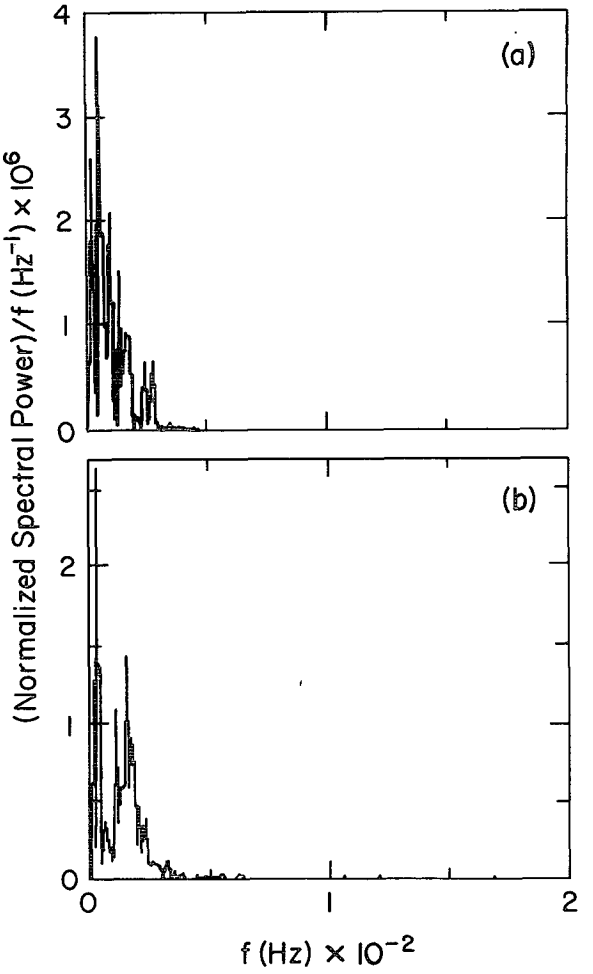

FIG. 6. Power spectra of microbarographs on 27 March 1981 (a) for 0720 MST and (b) for 0840 MST.

1981. Its direction and speed of propagation are generally southerly at 7–8 m s^{-1}. After 0800 MST a second wave component f_2 at $\sim 1.6 \times 10^{-3}$ Hz is evident as well, as shown in the spectral density plot for 0840 MST (Fig. 6b). Its speed of propagation—between 5 and 11 m s^{-1}—is similar to that of f_1 during this time period. Their directions of propagation, however, are quite different. While f_1 changes direction with time, f_2 propagates along the direction of the mean wind direction just above z_i. After 0940 MST f_2 continues to amplify while f_1 disappears as a discrete component.

The direction of propagation of the first wave component is opposite or perpendicular to the wind direction above the capping inversion. Therefore we believe that it is not associated with mixed-layer convection; rather, it possibly originates from a critical level aloft. The 0500 MST rawinsonde released from Denver, Colorado, indicates that a likely location for such a critical layer is in a strongly sheared region near 700 mb. The wind speed near the surface is

only about 1.5 m s^{-1}, while above 700 mb the wind speed increases to 19 m s^{-1}.

Figures 7a–c show the spectra of the vertical and horizontal velocity components at z/z_i = 0.13, 0.29 and 1.43 on 27 March 1981. The vertical velocity spectra at z/z_i = 0.13 and 0.29 contain more variance at higher frequencies than that at z/z_i = 1.43, while at lower frequencies they all have similar variance. At z/z_i = 1.43, the peak in the spectrum occurs at 2 $\times$ 10^{-3} Hz; at the lower two levels a local maximum also occurs at this frequency. There are also local maxima at 4 $\times$ 10^{-4} Hz (corresponding to the f_1 wave) at all three levels. The longitudinal and lateral velocity spectra are similar to the vertical velocity spectra at higher frequencies, but are considerably larger than the vertical at low frequencies. The large increase in the low-frequency energy of the longitudinal component above z_i seems to be due to contribution from waves.

The temperature spectra plotted in Fig. 7d also show that there is much more energy in the low frequency ($f < 0.05$ Hz) end of the spectra above z_i than there is below z_i. At high frequencies, the spectra are similar.

Caughey and Palmer (1979) reported spectral behavior that differed greatly within and above the mixed layer. They noted a large decrease in the high frequency spectral energy in the velocity components and in temperature, as well as a marked increase in spectral slope—becoming significantly steeper than $-\frac{2}{3}$ above the mixed layer. In our case, the slope does not change significantly from $-\frac{2}{3}$.

Figure 8 shows the normalized peak wavelength

$$\lambda_{m,w}/z_i = U_0/(f_{m,w}z_i),$$

where U_0 is the wind speed and $f_{m,w}$ is the peak frequency in the vertical velocity spectra. We note that $\lambda_{m,w}$ is nearly constant with height in the mixed layer, consistent with the results of Kaimal *et al.* (1976), but different from those of Caughey and Wyngaard (1979), who found that $\lambda_{m,w}$ decreases rapidly with height in the upper part of the mixed layer. Above the mixed layer the value of $\lambda_{m,w}$ is almost two times larger than the mixed-layer value and is close to the wavelength of the second wave component discussed previously. Note that $\lambda_{m,w}$ in the mixed layer is about twice the value of 1.5 z_i observed by Kaimal *et al.* (1976). However, Nichols and LeMone (1980) also obtained a value of $\lambda_{m,w}$ greater than 1.5 z_i. In our case, strong subsidence and entrainment may be factors contributing to the broadening of the convective cells in these shallow boundary layers.

Figure 9 shows the cospectra and quadrature spectra of temperature and vertical velocity at z/z_i = 0.06 and 1.43. At z/z_i = 0.06 the cospectrum is positive and relatively continuous, and the quadrature spectrum is considerably smaller than the cospectrum, while at z/z_i = 1.43, the cospectrum is concentrated in a few spectral bands and has a net negative area,

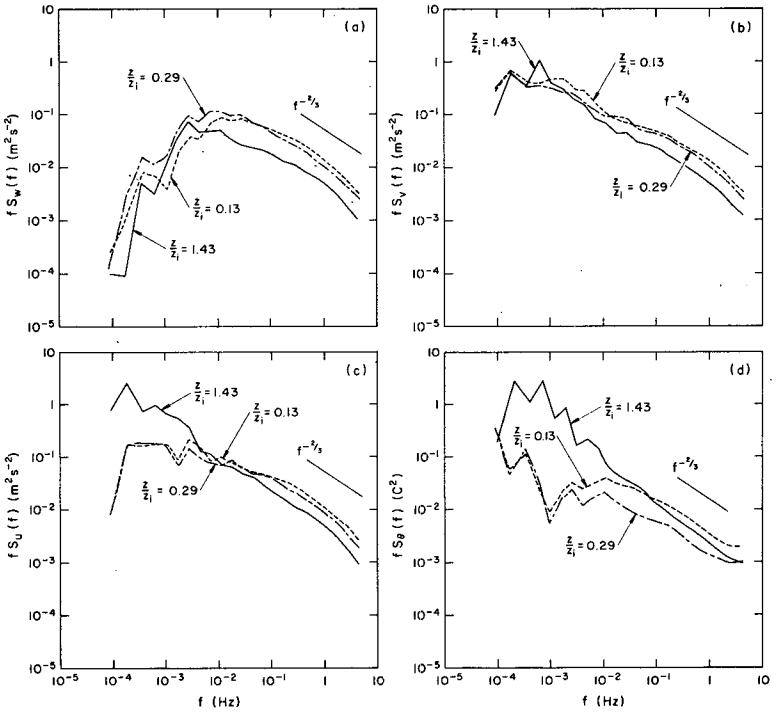

FIG. 7. Spectra of velocities and temperature for 0740 to 1040 MST 27 March 1981.

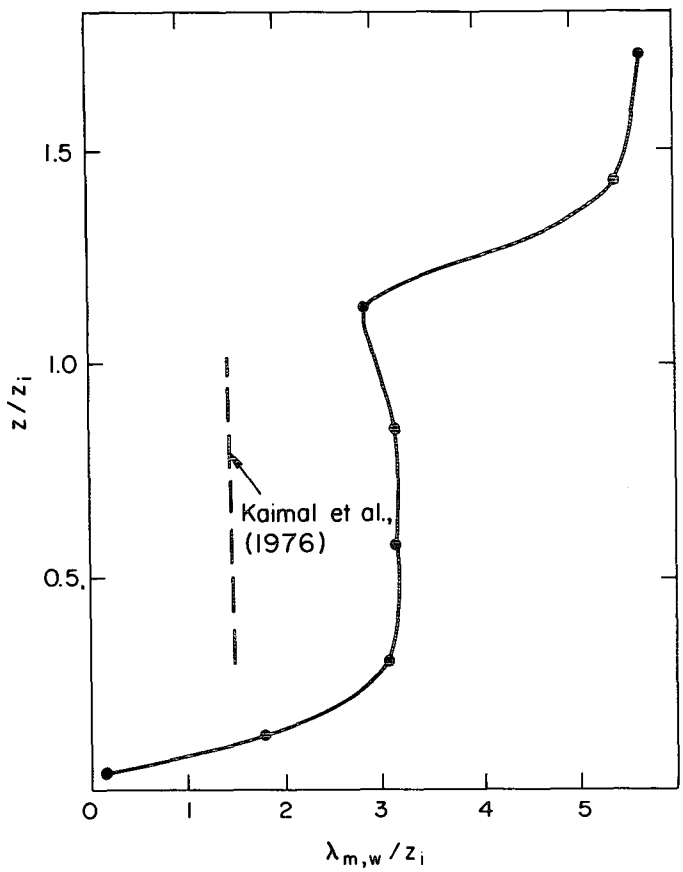

FIG. 8. Vertical distribution of normalized peak wavelength for the vertical velocity with z/z_i.

and the quadrature spectrum is larger than the co-spectrum.

To study the correlation in vertical motion between levels below and above z_i, we calculate the coherence between the vertical velocity at $z = 150$ m with the vertical velocity at levels below and above it. The coherence function $[\mathrm{Coh}_{w_z,w_{150}}(f)]^{1/2}$ and its phase angle are plotted in Fig. 10 for $f = 7.3 \times 10^{-3}$ Hz, which is the peak frequency of the w spectra in the middle of the mixed layer, and for $f = 5.6 \times 10^{-3}$ and 9.5×10^{-3} Hz, which are frequencies on either side of the peak frequency. We see that high coherence for $f = 7.3 \times 10^{-3}$ Hz exists not only between levels within the mixed layer, but also between the mixed layer and above. The phase angle is small in the mixed layer, but at the first two levels above the mixed layer w_z and w_{150} are nearly 90° out of phase. The coherences for $f = 5.6 \times 10^{-3}$ and 9.5×10^{-3} Hz are somewhat less than that for $f = 7.3 \times 10^{-3}$ Hz in the mixed layer, and very much less above z_i. Thus, we see a linkage between the boundary layer and the overlying atmosphere at the wavelength of the spectral maximum of w, while on either side of the maximum there is little or no correlation. We do not know, however, whether the boundary-layer turbulence is responding to forcing from above or vice versa.

5. Second-order moment budgets

In many of the aforementioned previous studies, terms in second-order moment budgets have been estimated, allowing a general understanding of their behavior in the convective boundary layer to be developed. We consider them here in order to compare ours with previous studies, and to indicate differences between these previous studies and the cases presented here. Complete data are available for second-order moment budgets only for 27 March 1981.

The turbulence kinetic energy budget is

$$\frac{\partial \bar{e}}{\partial t} = \underbrace{-\overline{uw}\frac{\partial U}{\partial z} - \overline{vw}\frac{\partial V}{\partial z}}_{S} \underbrace{- \frac{\overline{\partial we}}{\partial z}}_{T_r} - \frac{\overline{\partial pw}}{\partial z} \underbrace{+ \frac{g}{T}\overline{w\theta}}_{B} - \epsilon, \tag{7}$$

where p is the fluctuating kinematic pressure and the other notation is standard. Terms in the budget,

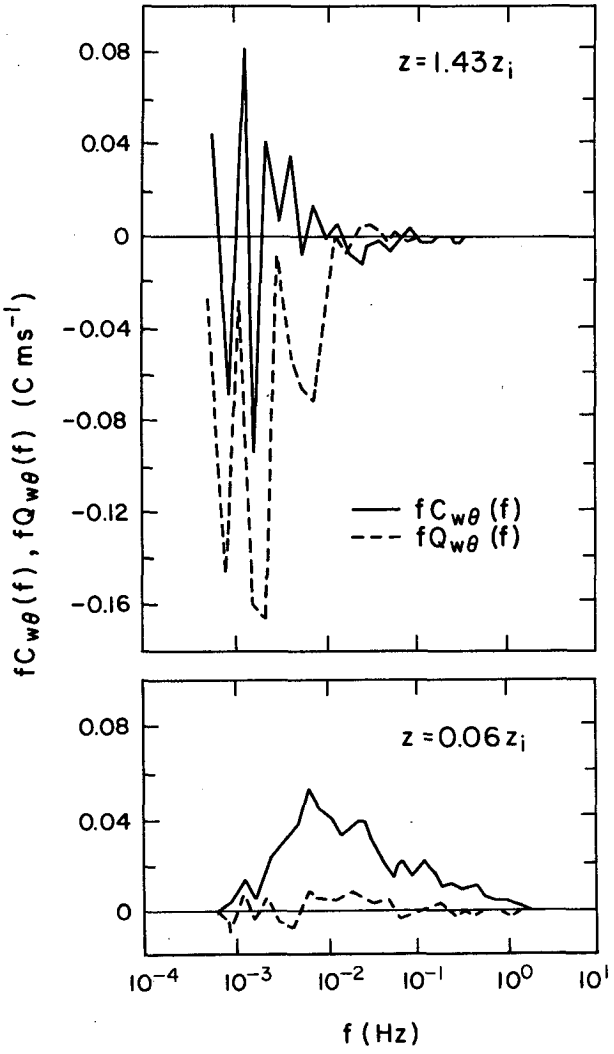

FIG. 9. Cospectra $C_{w\theta}(f)$ and quadrature spectra $Q_{w\theta}(f)$ of the heat flux at $z = 0.06z_i$ and $1.43z_i$ for 0840–0940 MST 27 March 1981.

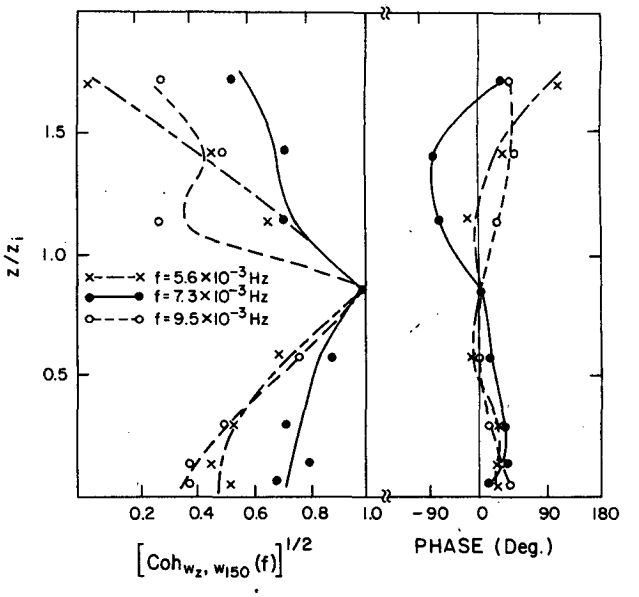

FIG. 10. Vertical distribution of $[\mathrm{coh}_{w_z,w_{150}}(f)]^{1/2}$ versus z/z_i for 0840–0940 MST 27 March 1981.

which are normalized by w_*^3/z_i, are shown in Fig. 11. In this and other second-order moment budgets, the time-derivative term is estimated from three successive 20 min period averages (0840–0940 MST), while the other terms are 1 h averages. The viscous dissipation is obtained from the inertial subrange of vertical velocity using a spectral constant of 0.67 (Kaimal *et al.*, 1976).

We note in Fig. 11, as well as in the other second-order moment budgets, that the time-derivative term is small in the mixed layer. About z_i, however, it increases with height and is significant for $z/z_i \approx 1.3$. The wind shear term S is negligible in the middle of the mixed layer but becomes the dominant source term near and above the top of the mixed layer. The turbulence energy flux divergence term T_r is the major source term in the upper part of the mixed layer but becomes the dominant loss term above the mixed layer. The pressure transport term was not measured and thus can only be estimated from the residual term. The buoyancy term B has a large negative value above z_i; in fact, if we considered only the temperature flux profile in estimating z_i, we would estimate a value of z_i about 1.3 times the value used here. Thus, the lapse rate becomes large well below the heat flux minimum because of the large downward temperature flux above and through the strong capping inversion—a direct consequence of the large shear production term in this region. The viscous dissipation term ϵ decreases with height through the bulk of the mixed layer, but remains important above the mixed layer.

Generally, the turbulence kinetic energy budget is typical of that found in previous studies in the lower part of the mixed layer. An exception is the transport term T_r near the surface, which is larger in magnitude

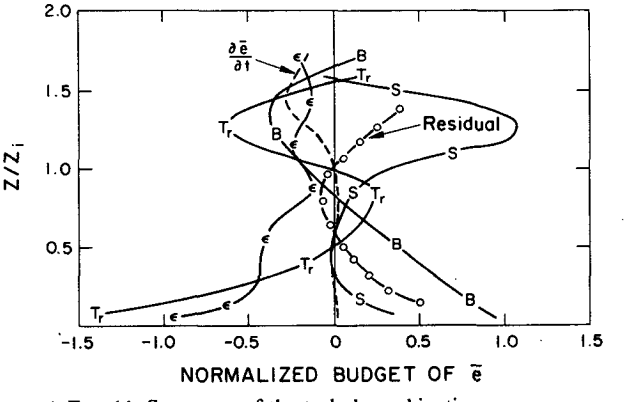

FIG. 11. Summary of the turbulence kinetic energy budget for 0840–0940 MST 27 March 1981.

than that observed in previous studies. However, near the top, shear becomes much more dominant than in previous studies. It is perhaps surprising that the mixed layer still maintains its integrity against the onslaught of shear-generated turbulence. However, instead of providing energy for entrainment, much of the shear-generated energy is transported upward by the turbulence transport term. At the same time, the residual term, which we associate with the pressure transport term, also increases in magnitude but is of opposite sign. This may be the result of pressure transport by wave motions. Carruthers and Hunt (1985) calculated that the energy flux $\overline{pw}$, induced by pressure fluctuations due to wave motions in a stratified layer, is related to the dimensionless buoyancy frequency N^*:

$$N^* = \frac{NL_H}{U_H}, \tag{8}$$

where

$$N = \left(\frac{g}{T}\frac{\partial\theta}{\partial z}\right)^{1/2},$$

L_H is the turbulent length scale, and U_H is the turbulent velocity scale. The value of $\overline{pw}$ is maximum when $N^* \approx 5$–6. If L_H and U_H are taken as $z_i/2$ and σ_H in the mixed layer, respectively, as in Carruthers and Hunt (1985), then at the capping inversion, $N^* \approx 6$. Although the value of N^* is at the predicted $\overline{pw}$ maximum, this may be somewhat fortuitous since the scales are only approximate, and Carruthers and Hunt assumed constant turbulence dissipation through the mixed layer and no vertical wind shear. Nevertheless, it seems likely that the contribution to $\overline{pw}$ by wave motions is significant. We cannot exclude the possibility, however, of significant contributions by advection to the residual.

The temperature variance budget reads

$$\frac{1}{2}\frac{\partial\overline{\theta^2}}{\partial t} = \underbrace{-\overline{w\theta}\frac{\partial\theta}{\partial z}}_{G} \underbrace{-\frac{1}{2}\frac{\partial\overline{w\theta^2}}{\partial z}}_{T_r} - \epsilon_\theta, \tag{9}$$

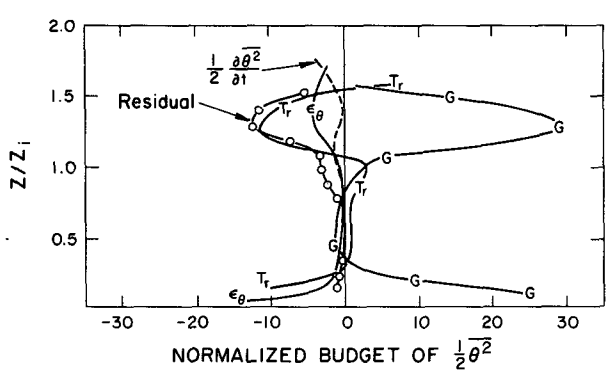

FIG. 12. As in Fig. 11 but for the temperature variance budget.

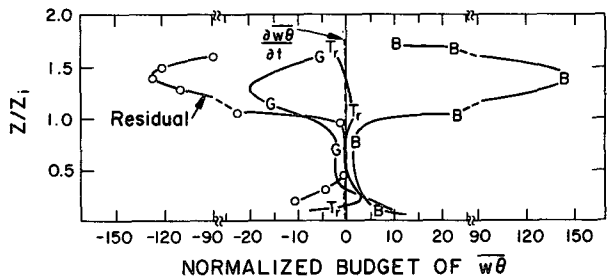

FIG. 13. As in Fig. 11 but for the temperature flux budget.

where ϵ_θ is the molecular destruction rate, which is estimated from the inertial subrange of the temperature spectrum using a spectral constant of 0.8 (Kaimal *et al.*, 1976). The terms normalized by $w_*\theta_*^2/z_i$ in (9) are shown in Fig. 12. Throughout the bulk of the mixed layer, the gradient production term G is somewhat larger than that reported by Lenschow *et al.* (1980), but it is consistent with the results of Deardorff's (1974) three-dimensional numerical simulations. We note that at $z/z_i = 1.3$ the gradient production term is very large, and is not balanced by loss terms. This suggests that horizontal advection may be important, since there are no unmeasured terms in this equation.

The temperature flux budget is

$$\frac{\partial\overline{w\theta}}{\partial t} = \underbrace{-\overline{w^2}\frac{\partial\theta}{\partial z}}_{G} \underbrace{-\frac{\partial\overline{w^2\theta}}{\partial z}}_{T_r} - \frac{\partial\overline{p}}{\partial z}\theta + \underbrace{\frac{g}{T}\overline{\theta^2}}_{B}. \tag{10}$$

The terms in the temperature flux equation, normalized by $w_*^2\theta_*/z_i$ with the exception of the pressure covariance term, which was not measured, are plotted in Fig. 13. We see that throughout the mixed layer the buoyancy term B, which is the main production term, is small compared with its value above z_i. The large value above z_i is not balanced by the gradient term G, which is a loss at this level. Therefore, we have a very large negative residual. The two possibilities that could account for this residual are the pressure covariance term and horizontal advection. The pressure covariance term is on the order of $\overline{w\theta}\sigma_w/\Delta h$ (Wyngaard, 1982), while horizontal advection is on the order of $\overline{w\theta}U/L_x$, where Δh is the inversion thickness and L_x a characteristic horizontal advection scale. For our case, $\sigma_w/\Delta h \approx 10^{-3}$ s^{-1}, while U/L_x is on the order of 10^{-4} s^{-1}. Therefore, we can conclude that the large negative residual necessary to balance the huge buoyant production rate is due primarily to the pressure covariance term. Deardorff (1974), in his numerical simulation of Wangara DAY 33, obtained similar profiles of the temperature flux budget terms in the mixed layer and also a maximum in the buoyancy term above z_i, but his maximum was less than 20% of ours and was nearly balanced by gradient production.

We noted earlier that the case studied here occurred during highly baroclinic conditions. This can be verified by means of the mean temperature budget. Neglecting the horizontal turbulence transport term, which is usually at least one order of magnitude less than the vertical turbulence transport term, the budget is

$$\frac{\partial \Theta}{\partial t} = -U\frac{\partial \Theta}{\partial x} - V\frac{\partial \Theta}{\partial y} - W\frac{\partial \Theta}{\partial z} - \underbrace{\frac{\partial \overline{w\theta}}{\partial z}}_{T_r}. \quad (11)$$

The time change and vertical flux divergence terms, which are normalized by $w_*\theta_*/z_i$, are shown in Fig. 14. In the mixed layer the residual, which is mainly mean horizontal advection, is negative. Estimating the mean horizontal wind speed at 4.1 m s^{-1}, the horizontal temperature gradient along the wind must be $\sim$0.12 C km^{-1}. Above z_i the residual is positive. This is probably the result of mean vertical advection of temperature, since this is a region of large subsidence with a strong inversion. In addition, the horizontal turbulence transport term may be significant above z_i.

An estimate of the mean horizontal temperature gradient can also be obtained from the momentum budget,

$$\frac{\partial U}{\partial t} = \lambda V - \lambda V_g - \frac{\partial \overline{uw}}{\partial z}. \quad (12)$$

$$\frac{\partial V}{\partial t} = \underbrace{-\lambda U}_{F} + \lambda U_g - \underbrace{\frac{\partial \overline{vw}}{\partial z}}_{T_r}, \quad (13)$$

where U_g and V_g are the geostrophic wind components in the x and y directions, respectively, and λ is the Coriolis parameter. Figure 15 shows the stress profiles normalized by u_* that were used to calculate T_r in (13). In the middle of the mixed layer, the stresses

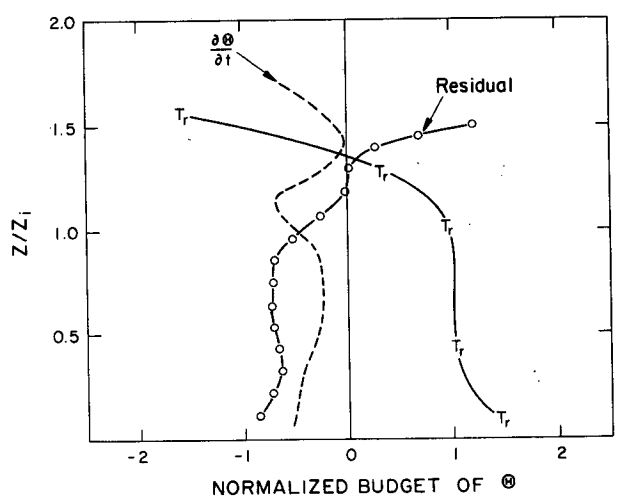

FIG. 14. As in Fig. 11 but for the mean temperature budget.

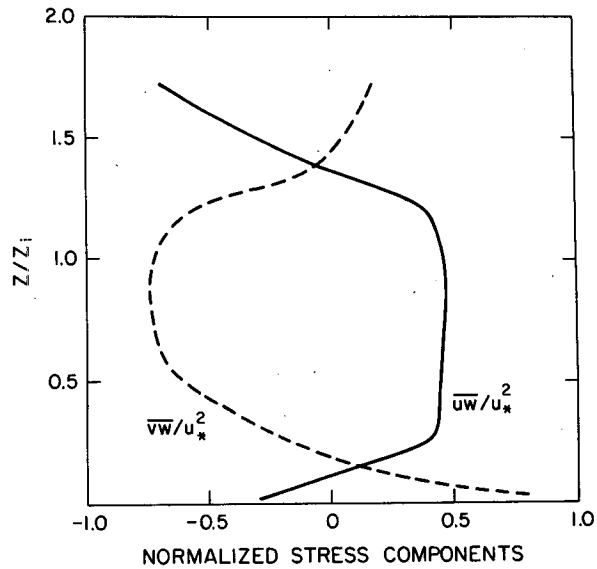

FIG. 15. Vertical distribution of normalized east and north stress components for 0840–0940 MST 27 March 1981.

are almost constant with height, while they vary considerably with height in the surface layer and above z_i. We note that the stress becomes small at $z/z_i \approx 1.3$, which corresponds to the level of maximum negative buoyancy flux, then increases in magnitude above this level. The terms in (12) and (13), except for the geostrophic wind terms, are normalized by u_*^2/z_i and plotted in Fig. 16. In the mixed layer, the residuals vary monotonically with height. The horizontal temperature gradient can then be obtained by means of the thermal wind relations,

$$\frac{\partial U_g}{\partial z} = -\frac{g}{T\lambda}\frac{\partial \theta}{\partial y}, \quad (14)$$

$$\frac{\partial V_g}{\partial z} = \frac{g}{T\lambda}\frac{\partial \theta}{\partial x}. \quad (15)$$

We estimate the horizontal temperature gradient to be $\sim$0.18°C km^{-1} at an azimuth angle of 214°; this gradient is somewhat higher than that estimated from the mean temperature budget. Although both these techniques for estimating the horizontal temperature gradient are only approximate, they do indicate that temperature advection is important, with a magnitude of about 0.5–0.7 $\times$ 10^{-3} °C s^{-1}. This is more than twice that reported by Lenschow *et al.* (1980) in the baroclinic boundary layer that forms during cold air outbreaks over the East China Sea.

6. Conclusion

Our analysis shows that, for the most part, the turbulence structure of the shallow baroclinic boundary layers considered here is consistent with previous studies of the convective boundary layer. However, the wavelength of the maximum in vertical velocity variance is about twice as large as in previous studies, and the turbulence structure in the vicinity of the

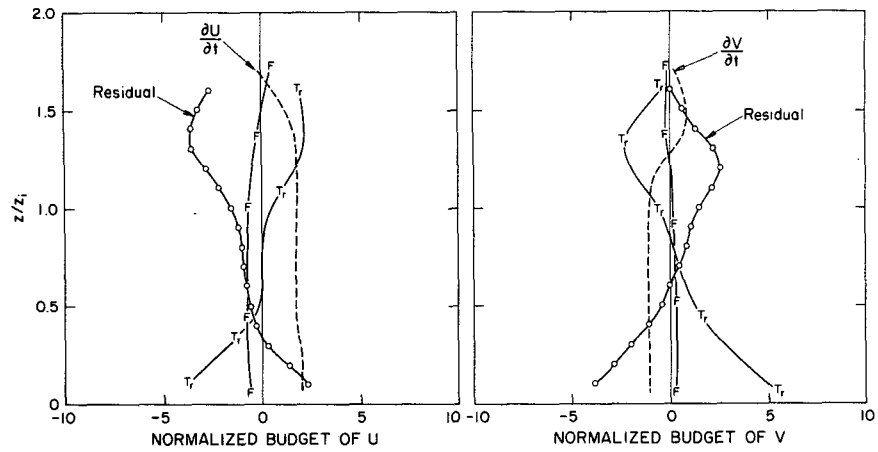

FIG. 16. As in Fig. 11 but for the mean momentum budget.

capping inversion is complicated by the relatively large production of turbulence energy by shear just above the mixed layer. As a result, a relative minimum of vertical velocity variance occurs at the top of the boundary layer. We have also shown that a linkage exists between vertical motions above and below the capping inversion.

Wind component and temperature spectra fit the expected $-\frac{2}{3}$ power law in the inertial subrange region of the spectrum within and above the boundary layer. Above the boundary layer, however, there is comparatively more energy in the low-frequency region of the spectra of horizontal wind components and temperature than within the boundary layer. Vertical velocity spectra are similar both within and above the boundary layer. However, the wavelength of the spectral maximum increases from about $3z_i$ within the boundary layer to about $5.5z_i$ above it.

For the most part, within the mixed layer, terms in the second-moment budgets agree with previous studies. Above z_i, however, many of the terms are much larger than within the mixed layer. The gradient production terms, in particular, are large source terms in the kinetic energy and temperature variance budgets, and a large sink term in the temperature flux budget. The transport, buoyancy, and dissipation terms in the kinetic energy budget are all negative above z_i, but still a significant positive residual exists. This may be due to pressure transport, although we cannot exclude the possibility of horizontal advection terms. Similarly, a large negative residual, which is due to the pressure covariance term, exists in the temperature flux budget above z_i.

Acknowledgments. The authors are grateful for useful discussions with J. J. Finnigan, J. C. R. Hunt, L. Kristensen, and J. C. Wyngaard. The authors also thank the reviewers for their helpful comments and H. Hamilton for typing the manuscript.

REFERENCES

Carruthers, D. J., and J. C. R. Hunt, 1985: Velocity fluctuation near an interface between a turbulent region and a stably stratified layer. *J. Fluid Mech.*, (in press).

Caughey, S. J., and S. G. Palmer, 1979: Some aspects of structure through the depth of the convective boundary layer. *Quart. J. Roy. Meteor. Soc.*, **105**, 811–827.

——, and J. C. Wyngaard, 1979: The turbulence kinetic energy budget in convective conditions. *Quart. J. Roy. Meteor. Soc.*, **105**, 231–239.

Deardorff, J. W., 1974: Three-dimensional numerical study of turbulence in an entraining mixed layer. *Boundary-Layer Meteor.*, **7**, 199–226.

Jensen, N. O., and D. H. Lenschow, 1978: An observational investigation of penetrative convection. *J. Atmos. Sci.*, **35**, 1924–1933.

Kaimal, J. C., and J. E. Gaynor, 1983: The Boulder Atmospheric Observatory. *J. Appl. Meteor.*, **22**, 863–880.

——, J. C. Wyngaard, D. A. Haugen, O. R. Coté, Y. Izumi, S. J. Caughey and C. J. Readings, 1976: Turbulence structure in the convective boundary layer. *J. Atmos. Sci.*, **33**, 2152–2169.

Lenschow, D. H., 1974: Model of the height variation of the turbulence kinetic energy budget in the unstable planetary boundary layer. *J. Atmos. Sci.*, **31**, 465–474.

——, J. C. Wyngaard and W. T. Pennell, 1980: Mean-field and second-moment budgets in a baroclinic, convective boundary layer. *J. Atmos. Sci.*, **37**, 1313–1326.

Mahrt, L., 1979: Penetrative convection at the top of a growing boundary layer. *Quart. J. Roy. Meteor. Soc.*, **105**, 469–485.

——, 1981: Circulations in a sheared inversion layer at the mixed layer top. *J. Meteor. Soc. Japan*, **59**, 238–241.

Moeng, C. H., 1984: A large-eddy simulation model for the study of planetary boundary-layer turbulence. *J. Atmos. Sci.*, **41**, 2052–2062.

——, and J. C. Wyngaard, 1984: Statistics of conservative scalars in the convective boundary layer. *J. Atmos. Sci.*, **41**, 3161–3169.

Nichols, S., and M. A. LeMone, 1980: The fair weather boundary layer in GATE: The relationship of subcloud fluxes and structure to the distribution and enhancement of cumulus clouds. *J. Atmos. Sci.*, **37**, 2051–2067.

Nieuwstadt, F. T. M., 1983: On the solution of the stationary, baroclinic Ekman-layer equations with a finite boundary-layer height. *Boundary-Layer Meteor.*, **26**, 377–390.

Wyngaard, J. C., 1982: Boundary-layer modeling. *Atmospheric Turbulence and Air Pollution Modeling*, F. T. M. Nieuwstadt and H. Van Dop, Eds., Reidel, 69–106.

——, and M. A. LeMone, 1980: Behavior of the refractive index-structure parameter in the entraining convective boundary layer. *J. Atmos. Sci.*, **37**, 1573–1585.

——, O. R. Coté and Y. Izumi, 1971: Local free convection, similarity, and the budgets of shear stress and heat flux. *J. Atmos. Sci.*, **28**, 1171–1182.

Young, J. M., and W. A. Hoyle, 1975: Computer programs for multi-dimensional spectra array processing. NOAA Tech. Rep. ERL 345-WPL 43, 35 pp.